Author Manuscript Author Manuscript Author Manuscript Author Manuscript

HHS Public Access
Author manuscript

J Phys Chem B. Author manuscript; available in PMC 2019 June 18.

Published in final edited form as:
J Phys Chem B. 2018 December 13; 122(49): 11488–11496. doi:10.1021/acs.jpcb.8b07414.

Dynamics of Quaternary Structure Transitions in R−State Carbonmonoxyhemoglobin Unveiled in Time-Resolved X−ray Scattering Patterns Following a Temperature Jump

Hyun Sun Cho[†], **Friedrich Schotte**[†], **Valentyn Stadnytskyi**[†], **Anthony DiChiara**[§], **Robert Henning**[‡], and **Philip Anfinrud**[*],[†]

[†]Laboratory of Chemical Physics, National Institute of Diabetes and Digestive and Kidney Diseases, National Institutes of Health, Bethesda, Maryland 220892-0520, United States

[§]Argonne National Laboratory, 9700 S. Cass Ave., Argonne, Illinois 60439, United States

[‡]Center for Advanced Radiation Sources, University of Chicago, Chicago, Illinois 60637, United States

Abstract

It is well-known that tetrameric hemoglobin binds ligands cooperatively by undergoing a ligand-induced T → R quaternary structure transition, a structure−function relationship that has long served as a model system for understanding allostery in proteins. However, kinetic studies of the reverse, R → T quaternary structure transition following photolysis of carbonmonoxyhemoglobin (HbCO) reveal complex behavior that may be better explained by the presence of two different R quaternary structures coexisting in thermal equilibrium. Indeed, we report here time-resolved small- and wide-angle X-ray scattering (SAXS/WAXS) patterns of HbCO following a temperature jump that not only provide unambiguous evidence for more than one R state, but also unveil the time scale for interconversion between them. Since the time scale for the photolysis-induced R → T transition is likely different for different R-states, this structural heterogeneity must be accounted for to properly explain the kinetic heterogeneity observed in time-resolved spectroscopic studies following photolysis of HbCO.

Graphical Abstract

---

[*]**Corresponding Author**: anfinrud@nih.gov (P.A.).

Notes
The authors declare no competing financial interest.

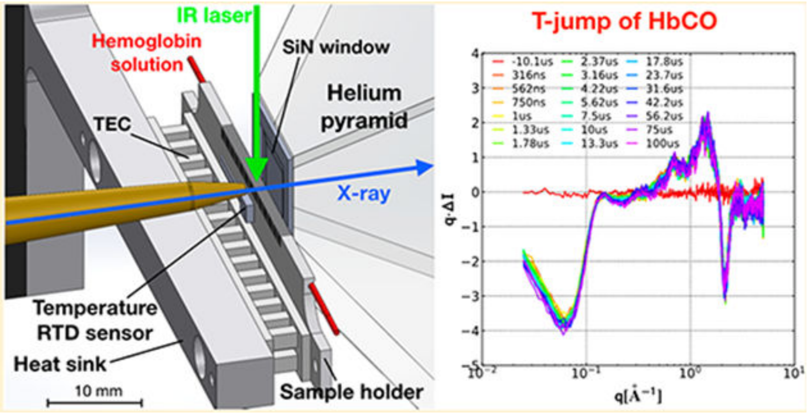

---

1. INTRODUCTION

Hemoglobin is a protein found in red blood cells that reversibly binds small ligands such as O_2, CO, and NO. It is comprised of two α-chains (141 amino acids each) and two β-chains (146 amino acids each), with each chain covalently linked to a ferrous heme that is capable of binding small ligands. It has long been known that the ligand-binding affinity of hemoglobin depends on its quaternary conformation (relative orientation of its α- and β-chains), with its so-called "Relaxed" R- and "Tense" T-states having high and low affinities, respectively.[1,2] When no ligands are bound, hemoglobin exists primarily in its "deoxy" T state (Hb), and when oxygen is bound to all four hemes, hemoglobin exists primarily in its "oxy" R state (HbO_2). Ligand dissociation from the high-affnity R state triggers a quaternary structure transition to the low-affnity T state, which significantly enhances the ability of hemoglobin to transport oxygen from the lungs to the tissues. This structure−function relationship has long served as a model system for understanding allostery in proteins.[1−9]

Though oxygen is hemoglobin's intended target, it also reversibly binds carbon monoxide to form HbCO, which is more stable than HbO_2, and can be photodissociated with high quantum yield using visible light. Thus, photolysis of HbCO with a short-duration laser pulse can trigger an R → T quaternary structure transition,[10] whose dynamics can be studied by various pump−probe methods. For example, pioneering time-resolved spectroscopic studies pursued by Eaton and co-workers identified a Soret band signature for the R → T quaternary structure transition, and concluded that this transition occurs with a time constant of about 20 μs.[11,12] They also observed a submicrosecond event that was attributed to a tertiary structure change. Subsequent time-resolved optical studies by Kliger and co-workers[13] reported a 38 μs time constant for the R → T structure transition, but also found a 1 μs relaxation that they attributed to an initial step along a compound R → T reaction pathway. Spiro and co-workers[14,15] studied the R → T transition with UV resonance Raman spectroscopy, and attributed fast (2.9 μs) and slow (21 μs) events to a stepwise quaternary structure transition. Subsequent resonance Raman studies of a hybrid hemoglobin, in which nickel replaced iron in the β-chains, concluded that the T quaternary conformation develops with a ~ 20 μs time constant.[16] Time-resolved circular dichroism and magnetic circular dichroism studies[17,18] also concluded that the R → T transition proceeds in a stepwise fashion, with the first ~2 μs step creating an obligatory allosteric intermediate

Author Manuscript
Author Manuscript
Author Manuscript
Author Manuscript

Author Manuscript
Author Manuscript
Author Manuscript
Author Manuscript

whose rate-limited transition to the equilibrium T state entails "⋯larger changes in protein conformation than occur in the primary step." The consensus view emerging from spectroscopic studies, which probe the R → T quaternary structure transition indirectly via spatially localized chromophores in the protein, is that this transition evolves in a stepwise fashion with characteristic fast and slow time constants of ~2 μs and ~20 μs, respectively. More recently, the R → T transition was studied with time-resolved wide-angle X-ray scattering,[19,20] a technique that is sensitive to changes in both local and global protein structure. These investigations reported both fast (~2 μs) and slow (~20 μs) events, similar to the spectroscopic results, but concluded that the main structural transition occurs on the fast time scale, while the slow component corresponds to small and localized structure changes. This interpretation contradicts spectroscopic studies which assumed, not unreasonably, that a larger amplitude conformational change occurs during the rate limited, slower step. Thus, a structural interpretation for the observed fast and slow processes remains controversial.

The kinetic models used to account for time-resolved spectroscopic and X-ray scattering data have all assumed HbCO exists in a single R quaternary state, and have rationalized the fast and slow processes observed in the context of a stepwise path along the reaction coordinate. Alternatively, might the heterogeneous kinetics observed along the R → T pathway be due to a heterogeneous mixture of two or more R states, with each having a different barrier for the R → T transition, and hence, different transition rates? Consistent with this possibility, NMR studies of HbCO in solution[21–24] reported a time-averaged quaternary structure that is intermediate between the R and R2 X-ray structures, and concluded that this structure likely represents an average over multiple states; e.g., it may represent a dynamic equilibrium between R and R2. These two crystal structures represent a subset of quaternary structures found for hemoglobin. For example, Dey et al. surveyed human hemoglobin crystal structures from 160 PDB entries[25] and found that the geometric arrangement of $\alpha-\beta$ dimers in deoxy hemoglobin structures cluster around one quaternary conformation (T-state), whereas liganded hemoglobin structures cluster primarily around R and R2 quaternary conformations. Liganded conformations outside the R and R2 clusters have been found with different crystallization conditions and have been denoted RR2, RR3, and R3. Since crystallographic R-states are more conformationally diverse than T-states, the possibility that HbCO in solution is in dynamic equilibrium between more than one R state is certainly plausible.

To properly interpret the complex kinetics uncovered in time-resolved studies of the R → T quaternary structure transition, it is crucial to know if HbCO exists in a single quaternary conformation, or is in dynamic equilibrium between two or more quaternary conformations. To that end, we developed the infrastructure required to pursue time-resolved small- and wide-angle X-ray scattering (SAXS/WAXS) studies[26] of proteins following a temperature jump (T-jump). Since the X-ray scattering pattern of a protein in solution is sensitive to its size and shape, a change in the scattering pattern following a T-jump would provide direct evidence for a shift in the equilibrium population of quaternary states. Indeed, the change in X-ray scattering observed following a T-jump in HbCO vs Hb provided unambiguous evidence for more than one R state in HbCO, but only one T state in Hb. Moreover, the time constant associated with interconversion between R states near 37 °C was found to be about 30 μs. Since this time constant is long compared to the fast component observed in time-

Author Manuscript

Author Manuscript

Author Manuscript

Author Manuscript

resolved studies of the R → T structure transition following photolysis of HbCO, one would expect the observed kinetics to be heterogeneous, and reflect two parallel R → T pathways. In light of this discovery, it is crucial to reinterpret the complex kinetics observed in time-resolved studies of the R → T transition with a model that accounts for R-state heterogeneity.

2. METHODS

2.1. Experimental Details.

We have developed the infrastructure required to pursue time-resolved SAXS/WAXS studies of proteins on the BioCARS 14-ID beamline[27] at the Advanced Photon Source in Argonne, IL, and used that capability to investigate structural dynamics in proteins on time scales as fast as 100 ps[26] and to investigate signaling in photoactive yellow protein.[28,29] Since that work, we have upgraded the BioCARS beamline with additional X-ray optics and other ancillary components. Briefly, the BioCARS beamline is equipped with two inline undulators (U23 and U27), white-beam slits, a heat-load chopper, a primary K-B mirror pair, a millisecond shutter, X-ray slits positioned on either side of a high-speed X-ray chopper, a secondary K-B mirror pair, a high-speed diffractometer to position samples, and a large area, high-speed X-ray detector. The X-ray shutter train (heat-load chopper, millisecond shutter, and high-speed chopper) is capable of transmitting, on demand, X-rays generated from a single bunch of electrons. The primary and secondary K-B mirrors control independently the vertical and horizontal dimension of the focused spot at the sample location, and can focus X-rays down to ~15 μm in either dimension.

For the SAXS/WAXS studies reported here, the undulator gaps and white beam slits were set to generate a 3% bandwidth (fwhm) “pink” beam peaked at 12 keV. With the synchrotron operating in hybrid mode, the X-ray shutter train was phased to transmit, on demand, X-rays generated from the super bunch (~317 nC, eight septuplets spanning 494 ns), and delivered ~3×10^{10} X-ray photons to the sample in a 40×40 μm spot at a repetition frequency up to 246 Hz.

The sample circulates through a thin-wall capillary (Figure 1) that is supported on a home-built, temperature-controlled, slotted BeO ceramic capillary holder, and positioned with a home-built, high-speed, XYZ diffractometer. To reduce X-ray scattering from the capillary, its ~40 μm wall thickness was HF-etched down to 10–15 μm; after etching, the inner surface was reacted with trichloro(1H,1H,2H,2H-perfluorooctyl)silane (Aldrich) to render it fluorophilic, which reduces the propensity of unfolded proteins to adhere to the inner wall. The partially transmissive beamstop is comprised of a 4.4 mm long aluminum cylinder that is bonded inside a tantalum sleeve, with both components machined from high-purity materials (Goodfellow). The transmitted X-ray photons generate a spot on the X-ray at the geometric center of the SAXS/WAXS scattering image. The integrated spot intensity is proportional to the incident X-ray flux and can be used as an internal standard to scale images acquired at different times. Given the ~90 mm spacing between the sample and partially transmissive beamstop, the 185.8 mm sample−detector distance, and the 340 mm square dimension of the X-ray detector, the scattering vector magnitude (q) accessible in the scattering images spans 0.02–5.2 Å^{-1}.

Author Manuscript Author Manuscript Author Manuscript Author Manuscript

Our home-built, third-generation field programmable gate array (FPGA) timing system controls operation of all time-sensitive components operating on the beamline including choppers, shutters, lasers, detectors, and motion control systems (details to be published elsewhere). Briefly, our FPGA has 24 configurable inputs/outputs and is capable of controlling the time delay between arrival of laser and X-ray pulses to a precision down to 11 ps.

Our home-built XYZ diffractometer (constructed with three Parker MX-80L linear motor translation stages), stepper-motor-controlled peristaltic pump (Clark 15KS), and millisecond shutter (oriented by Parker SM162AE-NMSN rotary servo motor) are connected to a multiaxis controller (Aerotech Ensemble EPAQ) that is programmed to slave the peristaltic pump operation and millisecond shutter rotation with translation of the capillary. The motion controller translates the capillary along its long axis to 41 predefined positions spaced by 0.61 mm, and the millisecond shutter transmits X-ray pulses prior to each step. After reaching the end of the forward stroke, the stage rapidly returns to its starting position and begins the next stroke. During the return stroke, the motion control system receives a bit-pattern-encoded message from the FPGA, which serves to synchronize motion of the stage and specify parameters that control the time sequence for multiaxis motion. The peristaltic pump remains stationary during the forward stroke, but displaces a user-selected volume during the return stroke. By translating the capillary between the arrival of consecutive X-ray and laser pulses, and intermittently pumping solution through the capillary with a peristaltic pump, the adverse effects of radiation damage with this high-flux X-ray source are well managed.

A high-precision temperature controller (ILX Lightwave LDT-5948) regulates current flowing through a TEC (Custom Thermoelectric) that is bonded to a custom-fabricated, slotted BeO ceramic substrate (American Beryllia) on which the capillary is supported. This ceramic material was selected for three reasons: (1) its thermal conductivity is high (~70% that of Cu); (2) its thermal expansion is similar to alumina, which simplifies bonding to the alumina surface on the TEC; (3) being a white ceramic, it is resistant to laser ablation at the high power densities used in time-resolved studies (laser ablation from early prototypes fabricated with anodized aluminum caused excessive scattering from the capillary due to condensation of ablation byproducts on the capillary). A water chiller (Oasis 160) circulates fluid through a heat sink bonded to the opposite side of the TEC. The temperature controller stabilizes the average temperature across the ceramic support to within a few milli-kelvin of the set temperature. Thanks to the small dead volume in the small-bore capillary and the closed-loop circulation system, static and time-resolved SAXS/WAXS studies can be pursued with 125-μL sample volume. Pressurization of the sample to 3 atm minimizes risk of gas bubble formation in the sample capillary during data collection.

Time-resolved SAXS/WAXS images were acquired with near-IR laser heating pulses focused to an elliptical spot on the capillary from above using a combination of cylindrical and spherical optics. The long axis was aligned along the direction of the X-ray beam and orthogonal to the long axis of the capillary. For these measurements, the stage was operated in stepping-48 mode (stage steps 0.61 mm every ~48 ms), the high-speed chopper transmitted the super bunch from hybrid mode (accounting for 84% of the ring current), and

Author Manuscript Author Manuscript Author Manuscript Author Manuscript

the X-ray intensity from 1 stroke (41 X-ray openings per stroke) was integrated on the detector before triggering its readout. Scattering images were acquired with the laser/X-ray time delay alternated between −10 μs and positive time points on a logarithmic scale. Because the thermal cooling rate of the capillary is comparable to the inverse of the period between strokes (~2.1 s), the steady-state temperature of the sample during T-jump data acquisition is elevated somewhat relative to the temperature controller set point. Keeping the laser firing during T-jump data acquisition ensures the sample offset temperature remains the same for all strokes integrated at each programmed time delay. Because the stage requires ~12 ms to step to the next position, the stepping-48 mode supports laser/X-ray time delays up to 36 ms.

The magnitude of the T-jump achieved is determined by the wavelength of the near-IR laser heating pulse, its power density, the capillary dimension, and where the X-ray beam passes through the capillary. For example, the height of the ~617-μm OD capillary was set so the X-ray beam passed through 150 μm below its top edge, which affords an X-ray path length of ~529 μm, and a laser penetration depth <150 μm.

Static SAXS/WAXS images were acquired at several fixed temperatures, or while ramping the sample temperature between minimum and maximum set points in 0.5 °C steps (T-ramp). The up and down ramps were typically repeated at least 3 times for each data set.

In spite of the relatively high protein concentration used in this study (~50 mg mL^{-1}), approximately 96% of the scattered photons detected correspond to buffer scatter. Hence, it is crucial to record buffer scatter in a separate experiment and, after appropriate scaling, subtract it from scattering recorded with protein in the buffer solution. Proper scaling requires knowledge of the integrated incident X-ray flux for each image, which is determined by analyzing the signal from a large area, X-ray sensitive, silicon PIN diode (Canberra ANFD300–20–300RM). This sensor is positioned downstream from a beryllium vacuum window mounted on the exit port of the high-speed chopper. It has a 4 mm diameter hole in the middle to pass the X-ray beam, but is sensitive to X-rays scattered from the beryllium window. Indeed, the number of hole-electron pairs generated from a single X-ray pulse corresponds to more than 10^6 12-keV photons. Therefore, the precision of the determination is limited by shot noise to be around 0.1%, which is significantly lower than the shot noise limit for the number of X-ray photons transmitted through the partially transmissive beamstop and detected by the Rayonix detector.

The signal from this PIN diode is recorded on a digital oscilloscope (LeCroy WaverRunner 606Zi) for every X-ray shot and analyzed off line to determine its integrated intensity. These integrated intensities are used to properly scale protein and buffer scattering curves before performing the buffer subtraction.

2.2. Sample Preparation.

Hemoglobin was isolated from red blood cells as described previously,[30] exchanged with 50 mM Tris-HCl buffer (150 mM NaCl; pH 7.4), concentrated to 50 mg mL^{-1} in a centrifugal concentration filter tube, converted to the cyanomet form (HbCN) and stored at 4 °C. To prepare fresh Hb or HbCO solutions, an aliquot of HbCN was injected into a vial that was purged with helium or CO; a slight molar excess of sodium dithionite was added to reduce the ferric Hb to ferrous, which generated deoxy hemoglobin (Hb) or carbonmonoxy hemoglobin (HbCO), respectively. The samples were passed through a 0.2 μm filter before injecting a 125 μL aliquot into a 0.5 mL V-bottom vial that was purged with an appropriate gas; this vial functions as a reservoir in our small dead volume, closed-loop circulation system.

2.3. Data Reduction.

Diffraction images were acquired with the Rayonix MX340-HS detector configured for 2 × 2 binning (3840 × 3840 pixels with a nominal size of 89 μm). A mask was applied to defective pixels and pixels affected by the beamstop. After subtracting the detector offset (10 counts), the pixels were rescaled to correct for the effects of polarization, absorption, and detector nonuniformity. The scattering vector magnitude (q) for each pixel was calculated and used to sort the pixels into bins of width $\Delta q = 0.0025$. To remove zingers from the data, outliers were rejected from each bin according to statistical criteria ($>3\ \sigma$). After outlier rejection, the remaining paired data in each bin were least-squares fit to a straight line, whose value at the midpoint of the bin was assigned to the scattering intensity (I) for that value q.

All T-ramp and T-jump data were acquired with numerous repeats. The scattering patterns for each repeat were scaled according to the integrated X-ray intensity measured for each image, and the scaled repeats were averaged to generate scattering patterns with a high signal-to-noise ratio. Statistical analysis of the resulting patterns suggests that their experimental uncertainties are close to the shot noise limit over the full range of q.

2.4. Data Analysis.

The scattering patterns obtained from a protein solution, I(q), contain both protein and buffer contributions. The buffer contribution is assumed to be proportional to the separately recorded pure buffer scattering pattern, with the scale corresponding to its volume fraction in the protein solution.[31] The protein contribution to the scattering pattern is obtained by simple subtraction of the appropriately scaled buffer scattering. With this approach, the protein scattering pattern is everywhere positive and corresponds to scattering from protein plus its hydration shell.

3. RESULTS AND DISCUSSION

The volume fraction of hemoglobin at a solution concentration of 50 mg mL^{-1} is only about 3.7%. Therefore, only a small fraction of the photons impinging on the X-ray detector are scattered from protein. To isolate the protein contribution to the solution scattering patterns, it is crucial to characterize accurately the temperature dependence of buffer scatter. To that end, we acquire static SAXS/WAXS patterns of buffer solution over a broad range of temperatures and acquire time-resolved SAXS/WAXS scattering patterns of buffer over a broad range of time delays spaced linearly on a logarithmic time axis with −10 μs time points interleaved between them as a reference for differencing (see representative data in parts A and B of Figure 2). The static, temperature-dependent scattering patterns serve as a

Author Manuscript

Author Manuscript

Author Manuscript

Author Manuscript

calibrated reference that can be used to quantify the magnitude of the *T*-jump achieved, as well as the temperature offset that arises from repetitive heating of the sample volume during *T*-jump data acquisition. For example, with the experimental conditions used to generate the data in Figure 2B, the temperature offset was found to be about 2 °C, and the magnitude of the *T*-jump was found to be about 9 °C (see Figure 2C). The temperature stability of the volume probed by the X-ray pulse following the *T*-jump was found to be 0.06 °C rms out to 100 μs, after which the sample cooled back down to the offset temperature. The cooling dynamics are complex and involve thermal diffusion along longitudinal and transverse temperature gradients generated by the IR laser pulse (along the long axis of the sample capillary and along the direction of the laser beam, respectively), radiative heat exchange between the solution and the BeO ceramic capillary support, and conductive heat exchange between the surface of the capillary and the air surrounding it. Nevertheless, the cooling dynamics are well described by a 2-dimensional Gaussian diffusion model (dashed red curve in Figure 2C).

Temperature-dependent SAXS/WAXS patterns of HbCO solution, Hb solution, and their buffer were acquired. Though the buffer-subtracted protein scattering patterns recorded at two different temperatures appear to be superimposable (Figure 3, parts A and B), their difference reveals temperature-dependent differences in both HbCO and Hb scattering (Figure 3C). These differences can arise from changes in protein structure, changes in the hydration shell, or both. Though HbCO and Hb differ in quaternary conformation and mass (0.17% difference), their solvent accessible surface areas are expected to be quite similar; therefore, it is not unreasonable to assume that the temperature-dependent changes in their hydration shell are similar. Hence, the difference between the HbCO and Hb difference curves in Figure 3C should isolate scattering differences that arise from changes in protein structure. Indeed, the double difference pattern shown in Figure 3D (blue curve) unveils a scattering signature that exhibits oscillatory features over the same range of *q* as the (Hb − HbCO) scattering difference (red curve), which correspond to differences in quaternary structure (T vsR). Clearly, changing the temperature triggers a change in the average structure of the protein; however, these data alone do not inform us whether the structural change arises from HbCO, Hb, or both.

Time-resolved *T*-jump studies of HbCO and Hb show clearly that the structural changes observed in Figure 3D arise from HbCO, not Hb, and this suggests that HbCO exists in more than one quaternary structure. In support of this claim, Figure 4 presents time-resolved scattering difference patterns ($I_t - I_{-10\ \mu s}$) for HbCO and Hb solutions, their buffers, and their buffer-subtracted differences. Parts D and H of Figures 4 chart the short- (blue) and long-time (red) scattering patterns for HbCO and Hb, respectively. The fact that the overall scattering curves for Hb and HbCO are very similar suggests that the *T*-jump induced scattering differences are dominated by changes to the hydration shell, which should be similar for the same magnitude *T*-jump. However, there are clear differences in scattering over the range $0.1 < q < 1.0$, which is sensitive to the quaternary structure of the protein: the short- and long-time scattering patterns for Hb are virtually superimposable (Figure 4H), whereas the curves for HbCO reveal clear differences (Figure 4D).

Author Manuscript Author Manuscript Author Manuscript Author Manuscript

On the basis of these observations, we conclude that the average structure of T-state Hb is minimally affected by the T-jump, and the scattering differences observed are dominated by changes in its hydration shell. Since the time required for thermal equilibration between the protein and the surrounding buffer is short compared to our time resolution,[32] scattering differences arising from temperature-dependent changes to the hydration shell are expected to appear promptly and remain constant up until the sample cools back to its steady-state temperature. In contrast to Hb, the average structure of HbCO is clearly affected by the T-jump, and evolves from 1 to 100 μs.

Global analysis of the time-dependent scattering of HbCO employed a two-state model in which the scattering contribution from the hydration shell was assumed to appear promptly while the scattering contribution from the protein was assumed to evolve according to first-order kinetics (Figure 5). The scattering patterns extracted from the data using this model (Figure 5B) unveil the hydration shell (blue curve) and protein (red curve) contribution to the scattering, and the time-dependent best-fit amplitudes of these basis patterns to the data (Figure 5C) unveil the time scale over which the change in average structure occurs. Note that over the range$0.1 < q < 1.0$, the protein scattering pattern extracted from the time-resolved data (Figure 5B) is very similar to that extracted from the static, temperature-dependent scattering data (Figure 3D). Note also that the scattering pattern assigned to the hydration shell of Hb (green curve) is very similar to that assigned to the hydration shell of HbCO (blue curve). Given these results, we conclude that HbCO exists in two (or more) different quaternary conformations with different free-energy minima. These conformations are in thermal equilibrium with each other, with their relative populations determined by the forward and reverse rates for their interconversion. A sudden jump in temperature triggers a change in the equilibrium population of those conformations, with the measured relaxation rate $(30\ \mu s)^{-1}$ being equal to the sum of the forward and reverse rates for their interconversion.

The allosteric R → T quaternary structure transition in hemoglobin has been investigated over many decades by time-resolved techniques capable of tracking changes in protein structure following photolysis of R-state HbCO. The emerging consensus that the R → T quaternary structure transition occurs in ~20 μs at ambient temperature[11] was challenged by more recent time-resolved wide-angle X-ray scattering studies, which suggested this structure transition is an order of magnitude faster.[19,20] However, the kinetics for the appearance of a “T-like” Hb structure was complex and exhibited both fast and slow components. In spite of NMR evidence to the contrary,[21–23] prior time-resolved studies assumed that HbCO exists in one R-state, and interpreted their kinetic data accordingly. The time-resolved SAXS/WAXS results reported here show unambiguously that HbCO exists in more than one quaternary conformation. Moreover, we found that the rate of interconversion between R-state conformations near body temperature (~37 °C) is slower than reported rates for the photolysis-triggered R → T state transition at room temperature.[12] If we assume that HbCO exists in two different, slowly interconverting R quaternary conformations, the photolysis-triggered R → T state transition would involve two distinct reaction coordinates, and the appearance of T-state Hb would be biexponential with the relative amplitudes of the two rates reflecting the relative populations of the two quaternary R states.

Author Manuscript Author Manuscript Author Manuscript Author Manuscript

Although we found no evidence for multiple T-state conformations, we cannot exclude that possibility. For example, if multiple T-state conformations had the same free energy, thermodynamics tells us that their equilibrium populations would be equal and insensitive to changes in temperature. Therefore, our T-state observations are not inconsistent with prior studies which concluded that multiple structures exist in both R- and T-state hemoglobin.[8,33] However, our study imposes an additional constraint that such conformational heterogeneity minimally affects the free energy of the conformations. Consistent with this possibility, the root-mean square deviation (RMSD) between known crystallographic T-state structures (0.13−0.44 Å) is small relative to that for known R-states structures (1.1−1.9 Å).[8]

Since the relative population of different R-state HbCO conformations is temperature dependent, time-resolved *T*-jump studies pursued over a range of temperatures could provide quantitative information regarding their populations, and by comparing scattering patterns extracted from those data with theoretical scattering patterns from known X-ray structures of HbCO, it may prove possible to deduce which of those structures coexist in thermal equilibrium in solution. Armed with this information, it may also prove possible to identify the structural origins of the barriers that separate different quaternary structures, and provide a far more detailed mechanistic explanation for the functionally important allosteric quaternary structure transition in hemoglobin.

4. CONCLUSIONS

The static and time-resolved SAXS/WAXS studies reported here show unambiguously that HbCO coexists in at least two different R-state quaternary conformations. Moreover, the measured rate of thermal interconversion between these states at ~37 °C, $(30\ \mu s)^{-1}$, is slow compared to reported room-temperature rates for the photolysis-induced R → T quaternary structure transition in hemoglobin. Thus, R-state heterogeneity adds complexity to the dynamics for the photolysis-induced R → T transition, and must be included in kinetic models used to fit those time-resolved data. We are pursuing additional time-resolved T-jump and photolysis studies of HbCO as a function of temperature with an aim to identify which of the reported X-ray crystal structures of HbCO are most consistent with the scattering patterns extracted from these solution phase studies. Clearly, the classical two-structure allosteric description of hemoglobin needs to be revised to accommodate R-state conformational heterogeneity, which had been implicated in prior biophysical studies,and is unveiled here.

ACKNOWLEDGMENTS

We thank Prof. John S. Olson and Dr. Jayashree Soman for generously providing the human HbCO used in this investigation, and Bernard Howder, Jr., for machining many of the components required for this study. Use of the Advanced Photon Source was supported by the U.S. Department of Energy, Basic Energy Sciences, Office of Science, under Contract No. DE-AC02–06CH11357. Use of the BioCARS Sector 14 was also supported by the National Institutes of Health, National Institute of General Medical Sciences Grant R24GM111072. The time-resolved setup at Sector 14 was funded in part through a collaboration with Philip Anfinrud (NIH/NIDDK). This research was supported by the Intramural Research Program of the National Institute of Diabetes and Digestive and Kidney Diseases, National Institutes of Health.

Author Manuscript

Author Manuscript

Author Manuscript

Author Manuscript

REFERENCES

(1). Perutz MF Stereochemistry of Cooperative Effects in Haemoglobin. Nature 1970, 228, 726–739. [PubMed: 5528785]

(2). Monod J; Wyman J; Changeux JP On the Nature of Allosteric Transitions: A Plausible Model. J. Mol. Biol 1965, 12, 88–118. [PubMed: 14343300]

(3). Koshland DE Jr.; Nemethy G; Filmer D Comparison of Experimental Binding Data and Theoretical Models in Proteins Containing Subunits. Biochemistry 1966, 5, 365–385. [PubMed: 5938952]

(4). Szabo A; Karplus M A Mathematical Model for Structure-Function Relations in Hemoglobin. J. Mol. Biol 1972, 72, 163–197. [PubMed: 4648112]

(5). Yonetani T; Park SI; Tsuneshige A; Imai K; Kanaori K Global Allostery Model of Hemoglobin. Modulation of O_2 Affinity, Cooperativity, and Bohr Effect by Heterotropic Allosteric Effectors. J. Biol. Chem 2002, 277, 34508–34520. [PubMed: 12107163]

(6). Eaton WA; Henry ER; Hofrichter J; Bettati S; Viappiani C; Mozzarelli A Evolution of Allosteric Models for Hemoglobin. IUBMB Life 2007, 59, 586–599. [PubMed: 17701554]

(7). Viappiani C; Abbruzzetti S; Ronda L; Bettati S; Henry ER; Mozzarelli A; Eaton WA Experimental Basis for a New Allosteric Model for Multisubunit Proteins. Proc. Natl. Acad. Sci. U. S.A. 2014, 111, 12758–12763. [PubMed: 25139985]

(8). Yuan Y; Tam MF; Simplaceanu V; Ho C New Look at Hemoglobin Allostery. Chem. Rev 2015, 115, 1702–1724. [PubMed: 25607981]

(9). Esquerra RM; Bibi BM; Tipgunlakant P; Birukou I; Soman J; Olson JS; Kliger DS; Goldbeck RA Role of Heme Pocket Water in Allosteric Regulation of Ligand Reactivity in Human Hemoglobin. Biochemistry 2016, 55, 4005–4017. [PubMed: 27355904]

(10). Gibson QH The Photochemical Formation of a Quickly Reacting Form of Haemoglobin. Biochem. J 1959, 71, 293–303. [PubMed: 13628568]

(11). Hofrichter J; Sommer JH; Henry ER; Eaton WA Nanosecond Absorption Spectroscopy of Hemoglobin: Elementary Processes in Kinetic Cooperativity. Proc. Natl. Acad. Sci. U. S. A 1983, 80, 2235–2239. [PubMed: 6572974]

(12). Hofrichter J; Henry ER; Szabo A; Murray LP; Ansari A; Jones CM; Coletta M; Falcioni G; Brunori M; Eaton WA Dynamics of the Quaternary Conformational Change in Trout Hemoglobin. Biochemistry 1991, 30, 6583–6598. [PubMed: 2054357]

(13). Goldbeck RA; Paquette SJ; Bjorling SC; Kliger DS Allosteric Intermediates in Hemoglobin. 2. Kinetic Modeling of HbCO Photolysis. Biochemistry 1996, 35, 8628–8639. [PubMed: 8679625]

(14). Jayaraman V; Rodgers KR; Mukerji I; Spiro TG Hemoglobin Allostery: Resonance Raman Spectroscopy of Kinetic Intermediates. Science 1995, 269, 1843–1848. [PubMed: 7569921]

(15). Balakrishnan G; Case MA; Pevsner A; Zhao X; Tengroth C; McLendon GL; Spiro TG Time-Resolved Absorption and UV Resonance Raman Spectra Reveal Stepwise Formation of T Quaternary Contacts in the Allosteric Pathway of Hemoglobin. J. Mol. Biol 2004, 340, 843–856. [PubMed: 15223325]

(16). Yamada K; Ishikawa H; Mizuno M; Shibayama N; Mizutani Y Intersubunit Communication via Changes in Hemoglobin Quaternary Structures Revealed by Time-Resolved Resonance Raman Spectroscopy: Direct Observation of the Perutz Mechanism. J. Phys. Chem. B 2013, 117, 12461–12468. [PubMed: 24067234]

(17). Bjorling SC; Goldbeck RA; Paquette SJ; Milder SJ; Kliger DS Allosteric Intermediates in Hemoglobin. 1. Nanosecond Time-Resolved Circular Dichroism Spectroscopy. Biochemistry 1996, 35, 8619–8627. [PubMed: 8679624]

(18). Goldbeck RA; Esquerra RM; Kliger DS Hydrogen Bonding to Trp Beta37 Is the First Step in a Compound Pathway for Hemoglobin Allostery. J. Am. Chem. Soc 2002, 124, 7646–7647. [PubMed: 12083904]

(19). Cammarata M; Levantino M; Wulff M; Cupane A Unveiling the Timescale of the R-T Transition in Human Hemoglobin. J. Mol. Biol 2010, 400, 951–962. [PubMed: 20594962]

Author Manuscript

Author Manuscript

Author Manuscript

Author Manuscript

(20). Cammarata M; Levantino M; Schotte F; Anfinrud PA; Ewald F; Choi J; Cupane A; Wulff M; Ihee H Tracking the Structural Dynamics of Proteins in Solution Using Time-Resolved Wide-Angle X-Ray Scattering. Nat. Methods 2008, 5, 881–886. [PubMed: 18806790]

(21). Lukin JA; Kontaxis G; Simplaceanu V; Yuan Y; Bax A; Ho C Quaternary Structure of Hemoglobin in Solution. Proc. Natl. Acad. Sci. U. S. A 2003, 100, 517–520. [PubMed: 12525687]

(22). Gong Q; Simplaceanu V; Lukin JA; Giovannelli JL; Ho NT; Ho C Quaternary Structure of Carbonmonoxyhemoglobins in Solution: Structural Changes Induced by the Allosteric Effector Inositol Hexaphosphate. Biochemistry 2006, 45, 5140–5148. [PubMed: 16618103]

(23). Sahu SC; Simplaceanu V; Gong Q; Ho NT; Tian F; Prestegard JH; Ho C Insights into the Solution Structure of Human Deoxyhemoglobin in the Absence and Presence of an Allosteric Effector. Biochemistry 2007, 46, 9973–9980. [PubMed: 17691822]

(24). Fan JS; Zheng Y; Choy WY; Simplaceanu V; Ho NT; Ho C; Yang D Solution Structure and Dynamics of Human Hemoglobin in the Carbonmonoxy Form. Biochemistry 2013, 52, 5809–5820. [PubMed: 23901897]

(25). Dey S; Chakrabarti P; Janin J A Survey of Hemoglobin Quaternary Structures. Proteins: Struct., Funct., Genet. 2011, 79, 2861–2870. [PubMed: 21905111]

(26). Cho HS; Dashdorj N; Schotte F; Graber T; Henning R; Anfinrud P Protein Structural Dynamics in Solution Unveiled via 100-ps Time-Resolved X-Ray Scattering. Proc. Natl. Acad. Sci. U. S. A 2010, 107, 7281–7286. [PubMed: 20406909]

(27). Graber T; Anderson S; Brewer H; Chen YS; Cho HS; Dashdorj N; Henning RW; Kosheleva I; Macha G; Meron M; et al. Biocars: A Synchrotron Resource for Time-Resolved X-Ray Science. J. Synchrotron Radiat. 2011, 18, 658–670. [PubMed: 21685684]

(28). Cho HS; Schotte F; Dashdorj N; Kyndt J; Henning R; Anfinrud PA Picosecond Photobiology: Watching a Signaling Protein Function in Real Time via Time-Resolved Small- and Wide-Angle X-Ray Scattering. J. Am. Chem. Soc 2016, 138, 8815–8823. [PubMed: 27305463]

(29). Cho HS; Schotte F; Dashdorj N; Kyndt J; Anfinrud PA Probing Anisotropic Structure Changes in Proteins with Picosecond Time-Resolved Small-Angle X-Ray Scattering. J. Phys. Chem. B 2013, 117, 15825–15832. [PubMed: 24125473]

(30). Wiedermann BL; Olson JS Acceleration of Tetramer Formation by the Binding of Inositol Hexaphosphate to Hemoglobin Dimers. J. Biol. Chem 1975, 250, 5273–5275. [PubMed: 238984]

(31). Glatter O; Kratky O Small Angle X-Ray Scattering; Academic Press: London, 1982.

(32). Lian TQ; Locke B; Kholodenko Y; Hochstrasser RM Energy-Flow from Solute to Solvent Probed by Femtosecond IR Spectroscopy - Malachite Green and Heme Protein Solutions. J. Phys. Chem 1994, 98, 11648–11656.

(33). Makowski L; Bardhan J; Gore D; Lal J; Mandava S; Park S; Rodi DJ; Ho NT; Ho C; Fischetti RF WAXS Studies of the Structural Diversity of Hemoglobin in Solution. J. Mol. Biol 2011, 408, 909–921. [PubMed: 21420976]

Author Manuscript
Author Manuscript
Author Manuscript
Author Manuscript

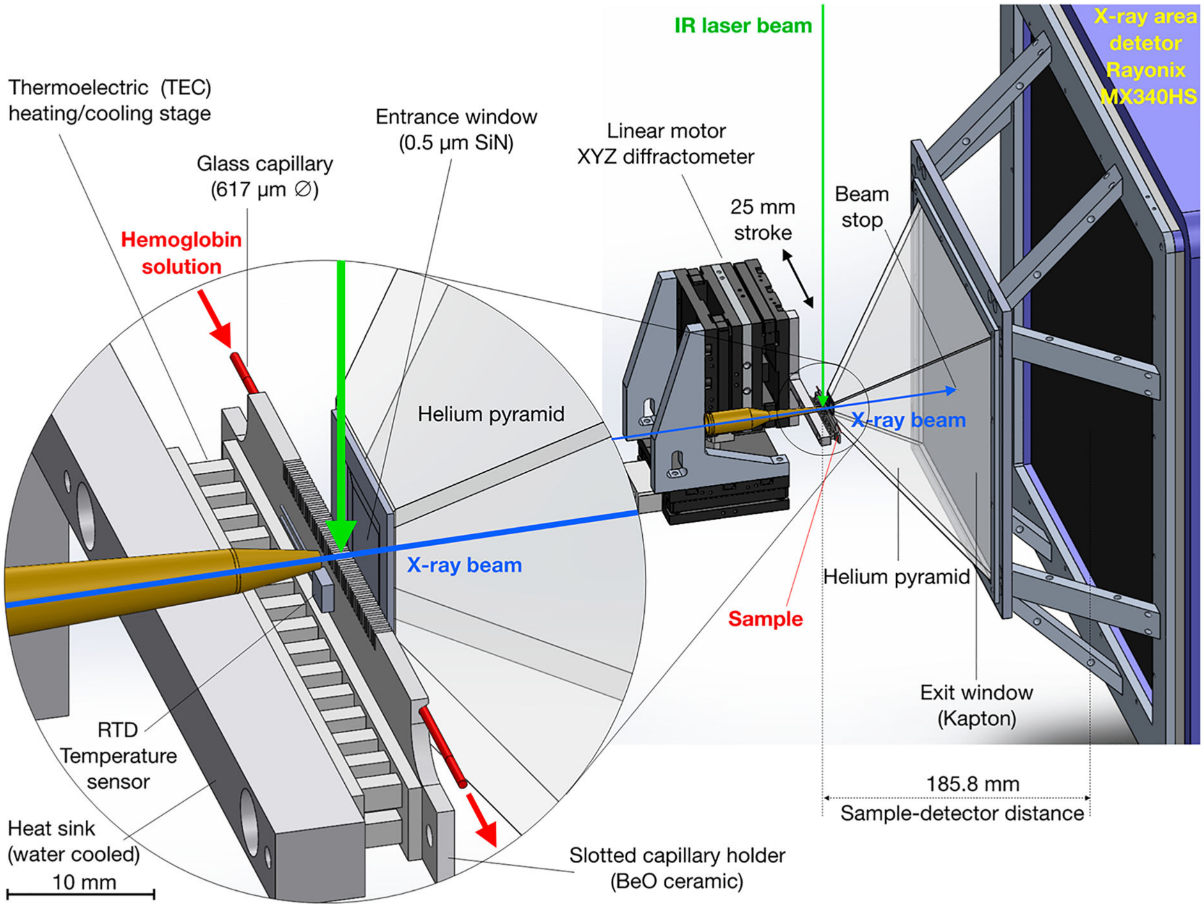

Figure 1.

Experimental geometry for acquiring time-resolved SAXS/WAXS images. An X-ray burst (12 keV; 3% fwhm; ~500 ns; ~3 × 10^{10} photons) passes through a 150-µm tungsten pinhole (not shown) located ~185 mm upstream from the capillary (red), continues through a brass collimator pipe with a 150-µm aperture tip, passes through a thin-wall, 617-µm diameter capillary (Polymicro TSP530660), enters a helium-purged pyramid through a 10 mm square, 0.5 µm thick SiN window (Norcada), and impinges on the center of a 0.51 mm diameter, partially transmissive beamstop that is attached to a Kapton film ~90 mm downstream from the capillary. A peristaltic pump (not shown) circulates protein/buffer solution through the capillary, which is affxed to a slotted, BeO ceramic support that is thermoelectrically heated/cooled, and positioned by a compact, home-built, high-speed XYZ diffractometer. An IR laser pulse (Opotek Opolette 355; 1.443 µm; ~5 ns; ~1 mJ, 20.8 Hz) is directed downward through a lens tube that focuses it to an elliptical spot on the capillary (~44 mJ-mm^{-2}) and produces a localized temperature jump. The scattering pattern from an X-ray pulse passing through the transiently heated solution is recorded on a large-area, high-speed X-ray detector (Rayonix MX340-HS). The scattering vector magnitude accessible with this setup [$q = (4\pi/\lambda)\sin\theta$] spans the range 0.02−5.2 Å^{-1}.

Author Manuscript

Author Manuscript

Author Manuscript

Author Manuscript

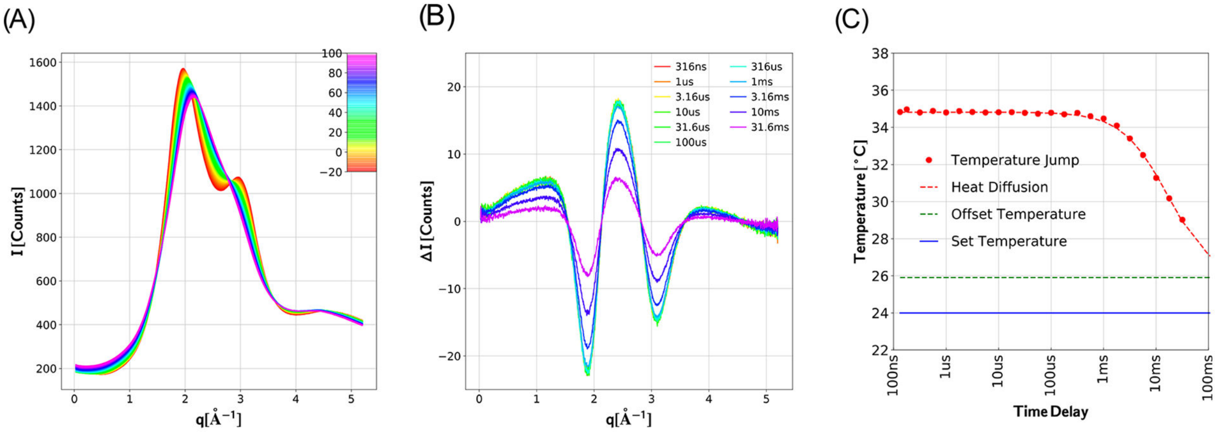

Figure 2.

Temperature-dependent SAXS/WAXS patterns are used to deduce the time-dependent temperature following a *T*-jump. (A) Temperature-dependent scattering patterns were acquired from aqueous buffer (150 mM NaCl, 20 mM acetate buffer, pH 4.9) over a broad range of q according to a T-ramp data acquisition protocol (see text). The intensity is reported in units of counts per pixel from a single image, with the color-coded curves representing the average of at least 6 images for each temperature. (B) Time-dependent scattering differences acquired following a 9 °C T-jump with the temperature controller set point programmed for 24 °C. ΔI corresponds to ($I_t - I_{-10\ \mu s}$), where I_{-10} μs represents the scattering pattern recorded with the X-ray pulse arriving 10 μs before the laser heating pulse. The amplitude of the scattering difference decreases at longer time delays as heat diffuses beyond the volume illuminated by the laser heating pulse. (C) Time-dependence of the buffer temperature within the volume probed by the X-ray beam following a 9 °C T-jump, as determined by using the curves in part A as a calibrated molecular thermometer. The temperature stability in the plateau region (t < 316 *μs*) was found to be 0.06 °C rms, which quantifies the precision of this “molecular thermometer.” The dashed red line corresponds to a 2-dimensional Gaussian diffusion model for thermal cooling at the laser beam center: $T(t) \propto [2\pi(2Dt + \sigma_L^2)]^{-1}$ where D is the diffusion constant and σ_L is laser spot size. The solid blue line corresponds to the temperature controller set point; the dashed green line corresponds to the solution temperature prior to the *T*-jump. Note that repetitive heating of solution in the sample capillary during *T*-jump measurements elevates its mean temperature about 2 °C relative to the temperature controller set point.

Author Manuscript Author Manuscript Author Manuscript Author Manuscript

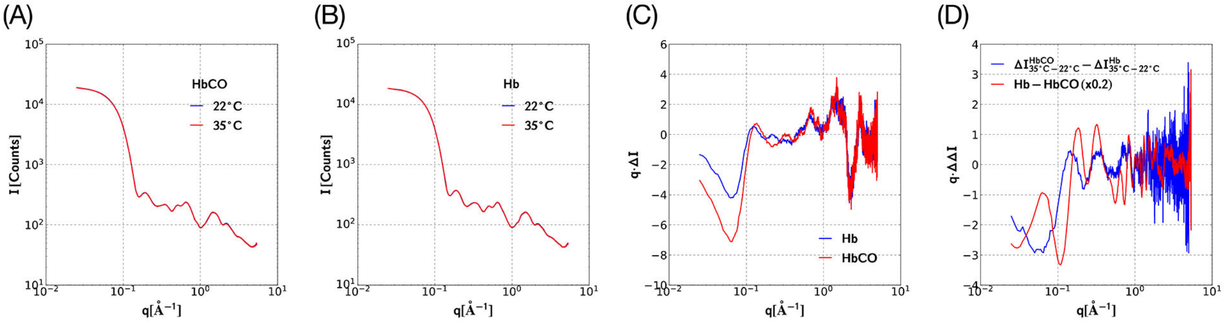

Figure 3.

Buffer-subtracted static SAXS/WAXS scattering of protein solution. (A) HbCO at two temperatures. (B) Hb at two temperatures. The scattering curves in panels A and B are nearly indistinguishable when plotted on a logarithmic scale. (C) Difference between high- and low-temperature curves for HbCO, from panel A, and Hb, from panel B. The observed differences are small, and arise from temperature-dependent scattering of the protein and/or its hydration shell. (D) The blue curve corresponds to the difference between the Hb (blue) and HbCO (red) curves shown in part C. This difference nominally subtracts the hydration shell contribution to the scattering difference, thereby unveiling the protein contribution to the scattering difference. The red curve corresponds to the scaled difference between the scattering curves shown in parts A and B, and it is included to illustrate the scattering difference between the quaternary conformations adopted by HbCO and Hb. Note the vertical axes in parts C and D correspond to $q \cdot \Delta I$, not ΔI, which facilitates visualization of both SAXS and WAXS regions on the same linear scale.

Author Manuscript

Author Manuscript

Author Manuscript

Author Manuscript

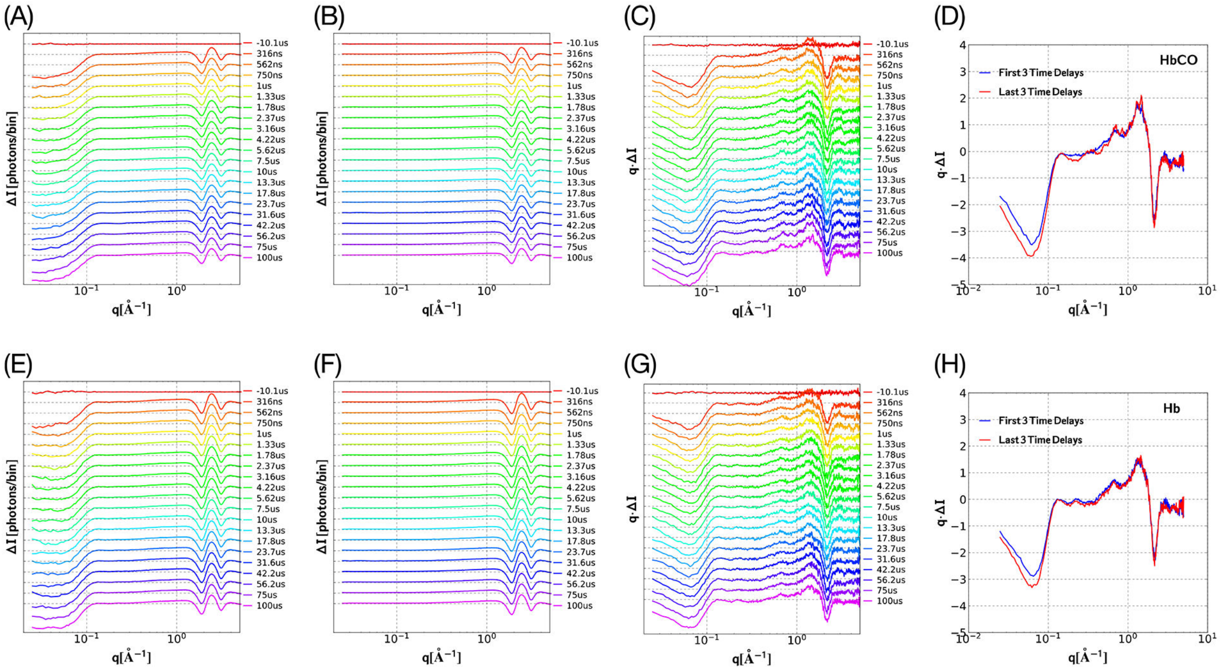

Figure 4.

Time-resolved SAXS/WAXS differences spanning 316 ns to 100 μs (8 time points per decade) following a T-jump; ΔI corresponds to ($I_t - I_{-10\ \mu s}$). (A) HbCO solution (22 °C set point; 1.3 °C offset; 13.5 °C T-jump). (B) Buffer under identical experimental conditions. (C) HbCO solution minus buffer. (D) Average scattering for the first three (blue) and last three (red) curves in the time series shown in part C. (E−H) Same as parts A−D but for Hb solution. Note the vertical axes in parts C, D, G, and H correspond to q·ΔI, not ΔI, which facilitates visualization of both SAXS and WAXS regions on the same linear scale. Over the range $0.1 < q < 1.0$, the short- and long-time scattering patterns for HbCO (D) differ significantly, whereas the corresponding patterns for Hb (H) are very similar.

Author Manuscript

Author Manuscript

Author Manuscript

Author Manuscript

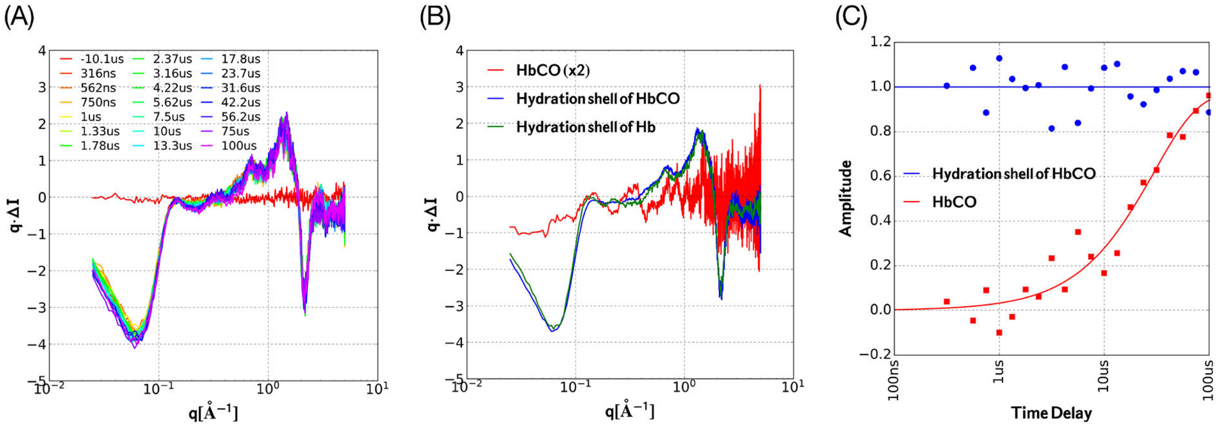

Figure 5.

Global analysis of time-dependent changes in the HbCO SAXS/WAXS pattern following a T-jump. (A) Time-resolved scattering curves (same as Figure 4C sans offset). (B) Scattering vectors extracted from a two-state model that reproduces the time-resolved scattering curves in part A with high fidelity. This model assumes the hydration shell contribution (blue) to the scattering difference is constant over the time range explored, and assumes the amplitude of the protein contribution (red) evolves according to first-order kinetics. For comparison, the scattering difference for Hb is shown (green). (C) Least-squares fit amplitudes of the two scattering vectors. The red solid curve corresponds to [1 - exp(−t/30 μs)] and tracks time-dependent changes of the protein scattering pattern. The blue curve is constant over time and corresponds to the hydration shell contribution to the scattering difference.